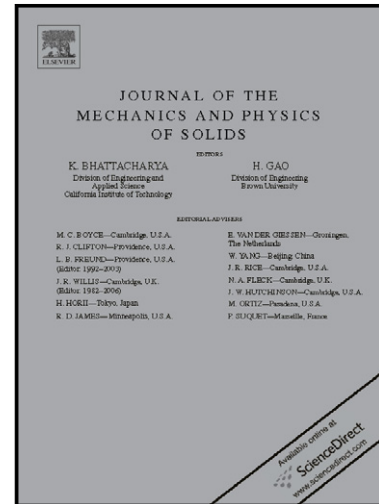


Author's Accepted Manuscript

Micromechanics of collective buckling in CNT turfs

Hamid Torabi, Harish Radhakrishnan, Sinisa Dj. Mesarovic



www.elsevier.com/locate/jmps

PII: S0022-5096(14)00147-1
DOI: <http://dx.doi.org/10.1016/j.jmps.2014.07.009>
Reference: MPS2512

To appear in: *Journal of the Mechanics and Physics of Solids*

Received date: 3 February 2014
Revised date: 2 May 2014
Accepted date: 22 July 2014

Cite this article as: Hamid Torabi, Harish Radhakrishnan, Sinisa Dj. Mesarovic, Micromechanics of collective buckling in CNT turfs, *Journal of the Mechanics and Physics of Solids*, <http://dx.doi.org/10.1016/j.jmps.2014.07.009>

This is a PDF file of an unedited manuscript that has been accepted for publication. As a service to our customers we are providing this early version of the manuscript. The manuscript will undergo copyediting, typesetting, and review of the resulting galley proof before it is published in its final citable form. Please note that during the production process errors may be discovered which could affect the content, and all legal disclaimers that apply to the journal pertain.

Micromechanics of collective buckling in CNT turfsHamid Torabi[¶], Harish Radhakrishnan[§], Sinisa Dj. Mesarovic^{¶*}[¶] School of Mechanical and Materials Engineering, Washington State University,
Pullman, WA 99164, USA[§] ANSYS, Inc., 15915 Katy Fwy, Suite 550, Houston TX 77084

* Corresponding author: mesarovic@mme.wsu.edu

Abstract

Complex structures consisting of intertwined, nominally vertical carbon nanotubes (CNTs) are called turfs. Under uniform compression experiments, CNT turfs exhibit irreversible collective buckling of a layer preceded by reorientation of CNT segments. Experimentally observed independence of the buckling stress and the buckling wavelength on the turf width suggests the existence of an intrinsic material length. To investigate the relationship the macroscopic material properties and the statistical parameters describing the nano-scale geometry of the turf (tortuosity, density and connectivity) we develop a nano-scale computational model, based on the representation of CNT segments as elastica finite elements with van der Waals interactions. The virtual turfs are generated by means of a constrained random walk algorithm and subsequent relaxation. The resulting computational model is robust and is capable of modeling the collective behavior of CNTs. We first establish the dependence of statistical parameters on the computational parameters used for turf generation, then establish relationships between post-buckling stress, initial elastic modulus and buckling wavelength on statistical turf parameters. Finally, we analyze the reorientation of buckling planes of individual CNTs during the collective buckling process.

Keywords: Discrete model; collective behavior; elastica; adhesive contact; intrinsic length

1. Introduction

While the remarkable mechanical, electrical and thermal properties of individual carbon nanotubes (CNTs) have been known¹, many applications depend on their collective behavior. CNT turfs are the assemblies of nominally vertical (grown from a substrate), but intertwined and slightly curved CNTs. They form a structure akin to open-cell foam and have unusual mechanical behavior². Applications of such structures include thermal switches (Christensen et al., 2003), nanoscale sensors³, hard disks and flat panel displays⁴.

The nano-scale geometry of a turf is the result of continuous energy minimization during the growth process, under substrate constraint and random influences. Two CNTs lower the energy by establishing contact bonds of the van der Waals type. Bending raises the energy. If CNTs were free during the growth process, the global energy minimum would be a dense bundle of straight tubes with maximum contact area. Growth being constrained by the substrate, the final configuration is a local energy minimum in configurational space (Mesarovic et al, 2007).

In applications, CNT turfs are subjected to different mechanical loads, whether as the part of the function, or by accident. Deformation changes the nanostructure of the turf and thus affects its properties, mechanical or otherwise. Therefore, understanding of the relationship between macroscopic mechanical properties and nano-scale geometry is of the paramount importance.

Under uniform compression, CNT turfs exhibit nonlocal behavior, with collective buckling of a layer⁵. The instability is characterized by the sharp maximum stress, followed by a stress drop. However, under non-uniform load such as sharp indentation, the turf exhibits stable visco-elastic deformation, with full mechanical reversibility up to very high strains⁶. It has been suggested that such behavior is the result of either non-homogenous properties of a material, or, a structure-like behavior, not describable by continuum mechanics (Cola et al., 2007; Hutchens et al., 2010). However, we have

¹ Ijima, 1991 Dresselhaus et al., 1996; Yakobson et al., 1996; Nardelli et al., 2000

² These are different from short widely spaced tubes (Qi et al., 2003; Waters et al., 2004).

³ Comini et al., 2002; Hahm and Lieber, 2004; Li et al., 2004; Bianchi et al., 2006

⁴ Chlebny et al., 1993; Wang et al., 2001; Ohgai et al., 2006; Arias, 2006

⁵ Cao et al., 2005; Zbib et al. 2008; Hutchens et al., 2010; Qiu et al., 2011a; Maschmann et al., 2011; Bradford et al., 2011

⁶ McCarter et al., 2006; Mesarovic et al. 2007; Qiu et al., 2011a, Radhakrishnan et al, 2013.

shown (Qiu et al., 2011a) that the variations in local mechanical properties of CNT turfs are negligible. Moreover, while the collective buckling is certainly a structural instability (in the sense that it depends on boundary conditions), the independence of the buckling stress and the buckling wavelength on the turf width (Zbib et al., 2008) indicates a continuum model with an intrinsic material length. A continuum model for stable behavior under non-uniform load has been developed recently in our group (Radhakrishnan et al., 2013).

To explain the collective buckling instability, Hutchens et al (2011) proposed a continuum model which exhibits localization and a stress drop, but without a characteristic material length scale. Consequently, their localizations are characterized by the size of computational cell. However, experimental results reported by our group (Zbib et al, 2008) demonstrate conclusively the necessity of the internal length scale in the process of collective buckling.

Computational models describing nano-scale behavior of CNT arrays include simple mass-spring models (Fraternali et al, 2011) and the models based on coarsened molecular dynamics, where segment of a CNT are treated as interacting particles⁷.

In this paper, we first develop the computational model based on CNT's bending and buckling as slender elastic rods, van der Waals normal interactions between the tubes, and a Coulomb-like frictional sliding. Upon implementing the model into the finite element framework, we analyze the behavior of the turf under uniform load. We demonstrate that the intrinsic length scale involved in the collective buckling arises from the statistical parameters characterizing the nano-scale geometry of the turf: tortuosity, density and connectivity, which will be defined later.

The paper is organized as follows. In Section 2, we discuss the governing equations of motions for an elastica followed by the interaction model between neighboring tubes. We define the constrained random walk algorithm used to generate a representative model of the turf in Section 3. Results and discussion are presented in Section 4. There, we focus on computational turf generation and the phenomenon of collective buckling in a CNT layer. The three aspects of the later are discussed: the

⁷ Buehler, 2006; Volkov et al., 2009; Anderson et al., 2010

buckling stress, the buckling wavelength and the mechanisms of collective buckling with oscillatory plane rotation. Summary and conclusions are given in Section 5.

2. Problem formulation

2.1 Governing equations

Kirchhoff's theory of inextensible elastic rods (Love, 1920, Antman, 1974), can be significantly simplified (Nordgren, 1974) if the cross section possesses rotational symmetry. Moreover, if the cross sectional diameter is much smaller than expected minimum radius of curvature, the strains will be small. It is instructive to re-derive Nordgren's (1974) equations from the energetic point of view, as such approach immediately provides the weak form and clarifies boundary conditions.

Deformation of an inextensible elastica is defined by the position vector of a material point $\mathbf{r}(s,t)$ (Figure 1) and the cross-sectional twist angle $\theta(s,t)$, where s denotes the arc length along the centerline in both reference and current configurations, and t is a time parameter of the deformation process. The unit tangent, normal and binormal vectors, $\hat{\mathbf{t}}$, $\hat{\mathbf{n}}$ and $\hat{\mathbf{b}}$, form the local orthonormal basis, and are defined as:

$$\hat{\mathbf{t}} = \mathbf{r}', \quad \kappa^2 = \mathbf{r}'' \cdot \mathbf{r}'', \quad \hat{\mathbf{n}} = \mathbf{r}''/\kappa, \quad \hat{\mathbf{b}} = \hat{\mathbf{t}} \times \hat{\mathbf{n}}. \quad (1)$$

$\kappa \geq 0$ is the curvature, primes denotes differentiation with respect to s : $\mathbf{r}' = d\mathbf{r}/ds$.

Small strain and in-plane isotropy of graphene sheets imply no torsion-bending coupling on the constitutive level, while small elastic strain implies linear constitutive equations.

Thus, we consider the internal energy density per unit length as a quadratic form of curvature and twist per unit length. Internal energy of an elastica segment of length L is then

$$U = \frac{1}{2} \int_0^L (B\kappa^2 + C\theta'^2) ds, \quad (2)$$

where B and C represent the bending and torsional stiffness, respectively.

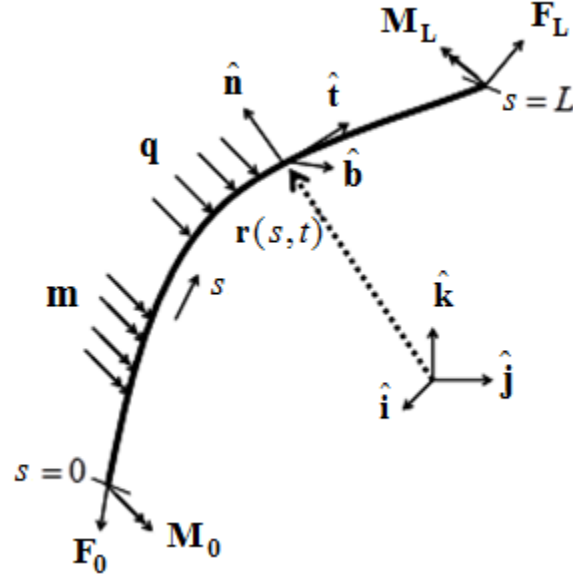


Figure 1. Schematic of an elastica segment subjected to distributed and end forces.

Nonlinear geometry produces torsion-bending coupling at the level of governing equations. Consider an infinitesimal segment ds (Figure 2), with curvature κ , loaded only with the torsional moments $H = \mathbf{M} \cdot \mathbf{r}'$. The resultant moment is $H\kappa ds \hat{\mathbf{n}}$, and it does work on the rotation about the normal, i.e., on the binormal components of the difference in displacements at the segment ends. The principle of virtual work (PVW) applied to such infinitesimal segment reads:

$$(B\kappa\delta\kappa + C\theta'\delta\theta')ds = -H(\mathbf{r}' \times \mathbf{r}'') \cdot \delta\mathbf{r}' ds. \quad (3)$$

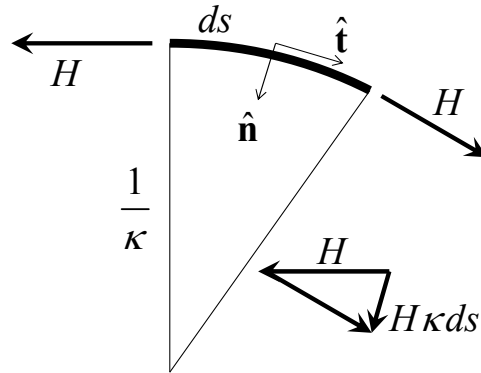


Figure 2. Equilibrium of torsional moments.

With the Lagrange multiplier λ enforcing the inextensibility condition $\mathbf{r}' \cdot \delta \mathbf{r}' = 0$, the PVW applied to the finite segment $[0, L]$

$$\int_0^L [B\kappa\delta\kappa + C\theta'\delta\theta' + H(\mathbf{r}' \times \mathbf{r}'') \cdot \delta \mathbf{r}' + \lambda \mathbf{r}' \cdot \delta \mathbf{r}'] ds = \int_0^L [(\mathbf{q} - \rho\ddot{\mathbf{r}}) \cdot \delta \mathbf{r} + (\mathbf{m} \times \mathbf{r}') \cdot \delta \mathbf{r}' + \mathbf{m} \cdot \mathbf{r}' \delta\theta] ds + [\mathbf{F} \cdot \delta \mathbf{r} + H\delta\theta + (\mathbf{M} \times \mathbf{r}') \cdot \delta \mathbf{r}']_0^L. \quad (4)$$

Here, $\ddot{\mathbf{r}}$ denotes acceleration, ρ is mass per unit length, and \mathbf{q} and \mathbf{m} are the distributed load and moment, while \mathbf{F} and \mathbf{M} are the cross-sectional force and moment (Figure 1).

Independent variations, $\delta \mathbf{r}$ and $\delta\theta$, yield two variational statements:

$$\int_0^L [B\mathbf{r}'' \cdot \delta \mathbf{r}'' + [H(\mathbf{r}' \times \mathbf{r}'') + \lambda \mathbf{r}' + (\mathbf{r}' \times \mathbf{m})] \cdot \delta \mathbf{r}' + (\rho\ddot{\mathbf{r}} - \mathbf{q}) \cdot \delta \mathbf{r}] ds = [\mathbf{F} \cdot \delta \mathbf{r} + (\mathbf{M} \times \mathbf{r}') \cdot \delta \mathbf{r}']_0^L, \quad (5)$$

$$\int_0^L [C\theta'\delta\theta' - \mathbf{m} \cdot \mathbf{r}' \delta\theta] ds = [H\delta\theta]_0^L. \quad (6)$$

This is the weak form of the problem.

The strong form of the problem is obtained by the standard procedure, with few caveats. From (6), we obtain

$$H' + \mathbf{m} \cdot \mathbf{r}' = 0 \quad \text{on } [0, L], \quad (7)$$

with boundary conditions either on $H = C\theta'$, or, on θ .

From (5), we obtain:

$$\int_0^L [B\mathbf{r}^{iv} + [H(\mathbf{r}' \times \mathbf{r}'') + \lambda \mathbf{r}' + (\mathbf{r}' \times \mathbf{m})]' + (\rho\ddot{\mathbf{r}} - \mathbf{q})] \cdot \delta \mathbf{r} ds = [\mathbf{F} + B\mathbf{r}''' - H(\mathbf{r}' \times \mathbf{r}'') - \lambda \mathbf{r}' - (\mathbf{r}' \times \mathbf{m})] \cdot \delta \mathbf{r} \Big|_0^L + (\mathbf{M} \times \mathbf{r}' - B\mathbf{r}'') \cdot \delta \mathbf{r}' \Big|_0^L. \quad (8)$$

The analysis of the boundary term with $\delta \mathbf{r}'$, together with the initial constitutive assumptions (2), reveal that

$$\mathbf{M} = B\kappa\hat{\mathbf{b}} + C\theta'\hat{\mathbf{t}}. \quad (9)$$

The analysis of the tangential component of the boundary term with $\delta \mathbf{r}$ yields the relationship between the Lagrange multiplier and the normal force $T = \mathbf{F} \cdot \mathbf{r}'$:

$$\lambda = T - B\kappa^2. \quad (10)$$

The remaining component of the same boundary term gives

$$\mathbf{F} = -B\mathbf{r}''' + H(\mathbf{r}' \times \mathbf{r}'') + \lambda\mathbf{r}' + (\mathbf{r}' \times \mathbf{m}). \quad (11)$$

The governing differential equation for $\mathbf{r}(s, t)$ is

$$B\mathbf{r}^{iv} + [H(\mathbf{r}' \times \mathbf{r}'') + \lambda\mathbf{r}' + (\mathbf{r}' \times \mathbf{m})]' - \mathbf{q} = -\rho\ddot{\mathbf{r}} \quad \text{on } [0, L]. \quad (12)$$

The number of independent boundary conditions on either $(\mathbf{r}, \mathbf{r}')$ or (\mathbf{F}, \mathbf{M}) is five, since the rotation/moment about the tangent are already taken into account as boundary conditions to (7).

Details of the finite element implementation are given in Appendix A.

2.2 Adhesive contact model

Experimental results reported in our group (Qiu et al., 2011b) demonstrate the rate-dependent behavior and time-relaxation of CNT turfs. Given the stable nature of covalent bonds within a CNT, the only possible mechanism for such behavior is the thermally activated creep of contacts. Thus, we assume that no covalent bonds form between the tubes, and that the interactions between the tubes are of the van der Waals type. The normal forces are then adequately described by Lennard-Jones pair potentials (Buehler, 2006) and can be adopted for a continuum model (Radhakrishnan and Mesarovic, 2009). The key assumption is that the normal force exerted by the segment B on a point of tube A (Figure 3a) is determined by the shortest distance from the point A to the segment B , and has the same direction, indicated by the unit vector $\hat{\mathbf{d}}$ in Figure 3a. Forces are computed at nodes by summing up all the interactions. The Lennard-Jones forces are short-ranged forces and are subject to cut-off distance beyond which interactions are negligible. A similar procedure is used to compute the Lennard-Jones interactions between the tubes and the indenter.

The Lennard–Jones force exerted on a node by a segment is given by

$$P(r) = \frac{24\varepsilon}{\sigma} \left[-2 \left(\frac{\sigma}{r} \right)^{13} + \left(\frac{\sigma}{r} \right)^7 \right], \quad (13)$$

where ε and σ are the Lennard–Jones parameters and r is the distance between the outer walls of the tubes. The values are given in Appendix B. The force law (13) is illustrated in Figure 3b.

Experimental observations in our group (Qiu et al., 2011b) also indicate relatively stable contacts at low forces. Such initial resistance to contact sliding is best taken into account by the Coulomb type friction law. For computational convenience, we use the viscous regularization of Coulomb friction. This model does not properly describe thermally activated contact sliding nor the rate-dependent behavior; it merely assures that contacts have certain strength, but can slide when that strength is exceeded. However, for numerical experiments with fixed loading rate, this is sufficient. It remains to determine the strength of the contact, i.e., the friction coefficient. We address this question in Appendix B.

The sliding friction force in Coulomb model is proportional to the normal force. However, the normal force (Figure 3b) changes sign. Moreover, it is expected that friction force becomes larger as the tubes approach, even to a distance smaller than r_0 where the normal reaches its maximum. For the friction model, we define the pseudo-normal force P_m , by linearly interpolating forces between r_0 and r_1 (Figure 3b), the latter being the inflection point on the force curve. The resulting pseudo-normal force, plotted in Figure 3c, has the cut-off at r_2 .

Let the relative velocity of points A and B in Figure 3a be $\mathbf{v} = \dot{\mathbf{r}}_A - \dot{\mathbf{r}}_B$. The sliding component is given as:

$$\mathbf{v}_s = \mathbf{v} - (\mathbf{v} \cdot \hat{\mathbf{d}})\hat{\mathbf{d}}, \quad (14)$$

The frictional force acting on point A in the direction opposite to \mathbf{v}_s is given by

$$P_s = \mu P_m(r) \left(\frac{|\mathbf{v}_s|}{v_0} \right)^\beta. \quad (15)$$

where μ is the friction coefficient, $P_m(r)$ is the pseudo-normal force, v_0 is the reference velocity taken as a fraction of the indentation velocity, and $\beta \ll 1$. Details are given in Appendix B.

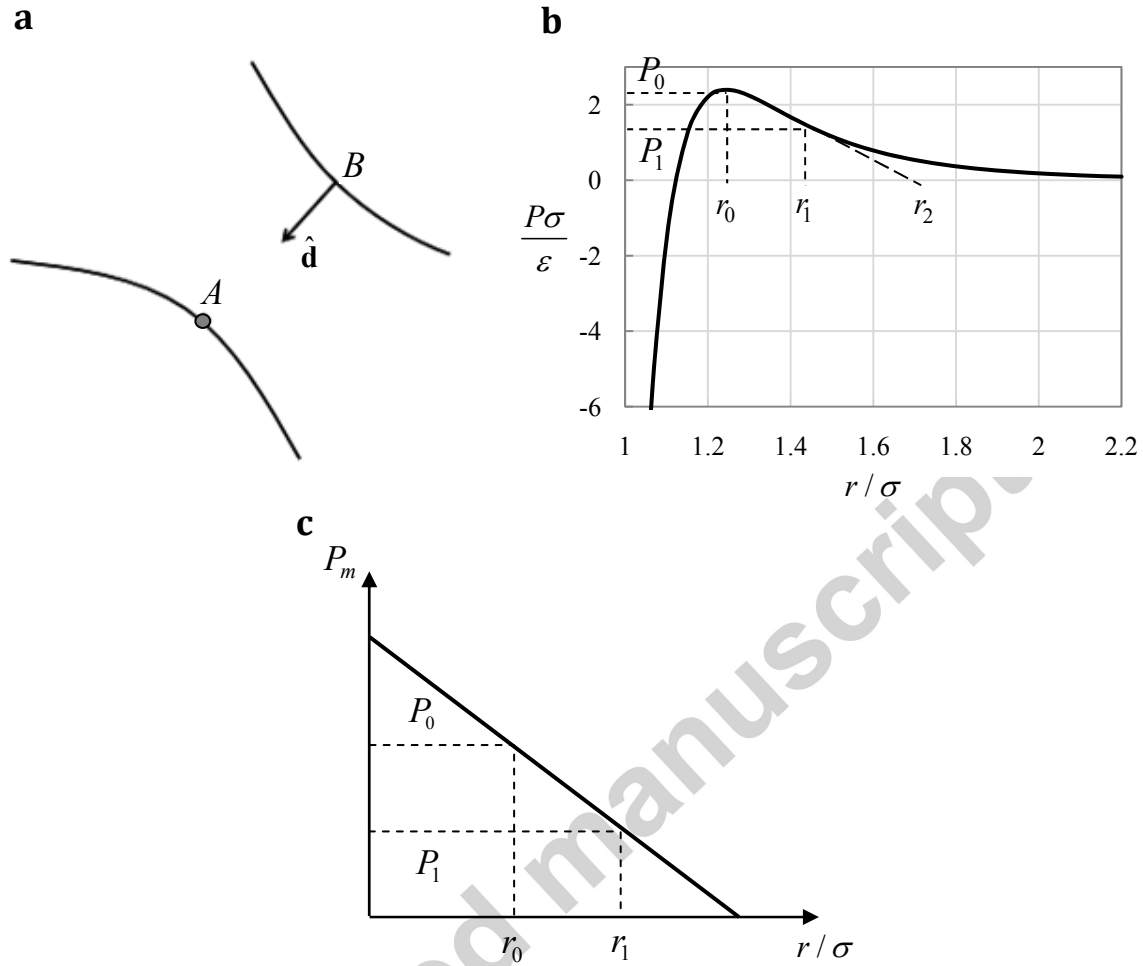


Figure 3. (a) Normal force on point A exerted by the neighboring segment. (b) Normalized force vs. normalized distance (13). r_0 is the distance where the adhesive force is maximum, r_1 is the distance where $P'' = 0$, and r_2 is the cut-off distance for the pseudo-normal force. (c) Pseudo-normal force vs. normalized distance.

3. Generation of the initial turf

In order to generate turfs similar to experimental ones, a *constrained random walk algorithm* is devised. Random seed points (x_0, y_0) are generated on the substrate $z = 0$. To prevent excessive clustering of the seeds, the minimum distance of 200 nm is enforced between every two seed points by rejecting the points which fall within this distance from previously generated points. Then, tubes are grown from the seeds in the random direction but within a limiting cone (Figure 4a), with the constant step w in the

z direction. The growth direction in each step is determined using randomly computed angles θ and ϕ so that the position of the points in the step n is given by

$$\begin{aligned} x_n &= x_{n-1} + w \cos \theta \sin \phi, \\ y_n &= y_{n-1} + w \sin \theta \sin \phi, \\ z_n &= z_{n-1} + w \cos \phi. \end{aligned} \quad \left(-\pi < \theta < \pi, \quad -\frac{\alpha}{2} < \phi < \frac{\alpha}{2}\right) \quad (16)$$

where α is the limiting cone angle. After generating the control points for each tube, cubic Hermite polynomials are fitted through in each segment, as follows.

Standard Hermit cubics require the nodal values of the function and derivatives (C^1 continuity). Since the latter is not available, we impose C^2 continuity at the nodes, and thus obtain the required number of conditions. Thus generated configuration of a CNT turf is illustrated in Figure 4b.

In order to mimic infinitely wide samples, periodic boundary conditions are enforced at all four sides of the unit cell in the x and y -direction. When a segment passes through one face of the cell, it is shifted and reappears on the opposite face. Figure 4c illustrates a periodic cell with tube segments in two colors. The red segments have remained in the cell. The blue segments have left the cell and were shifted by the period to re-enter the cell.

Thus generated turf is not in equilibrium. We allow it to relax for $0.2 \mu\text{s}$, under the elastic restoring forces and van der Waals interactions. In that interval the system reaches equilibrium state where the kinetic energy and the strain energy remain constant with time and stable contacts are formed.

The average curvature of each turf can be computed by

$$K = \frac{1}{L} \int_0^L |\kappa(s)| ds. \quad (17)$$

where L is the total length of nanotubes within a periodic cell. Each nanotube is discretized using 100 elastica elements, each approximately 100 nm, so that the total height of the turf is approximately $10 \mu\text{m}$. The initial and relaxed average curvatures for turfs with different cone angles and substrate sizes are listed in Table 1.

Number of tubes per area of the periodic cell determines the seed density of the turf sample. Turfs with three seed densities and three limiting cone angles are generated.

The seed density of 50 tubes in each 1 μm corresponds to experimental findings reported by Qiu et al. (2011).

Table 1. Average curvature (μm^{-1}) (before) after relaxation for CNT turfs.

Cone angle	Seed density (μm^{-2})		
	100	50	25
$\pi/2$	(0.644) 0.419	(0.627) 0.405	(0.626) 0.395
$\pi/3$	(0.452) 0.281	(0.443) 0.271	(0.440) 0.253
$\pi/4$	(0.351) 0.221	(0.336) 0.198	(0.333) 0.174

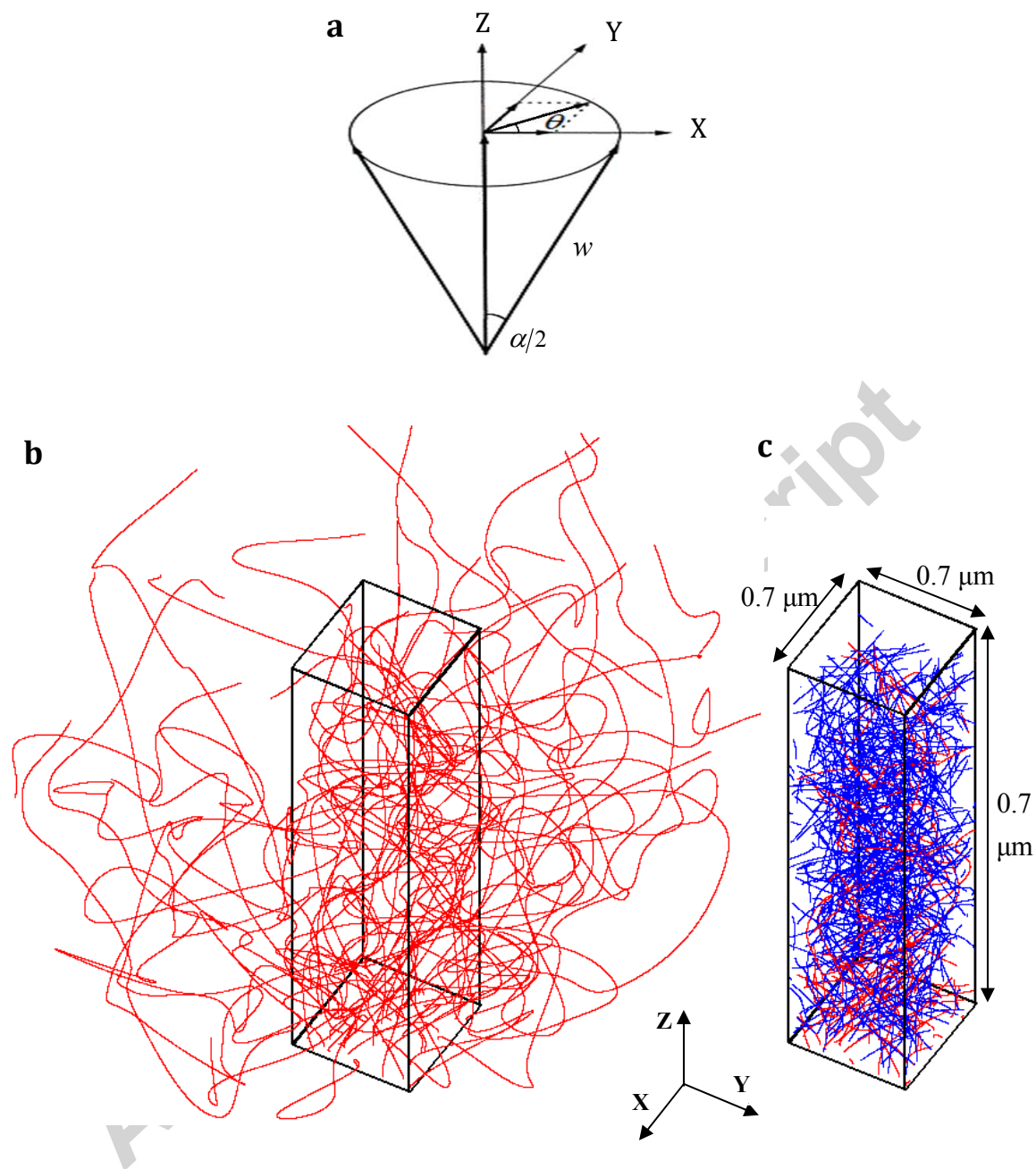


Figure 4. (a) Parameters for the constrained random walk (CRW) algorithm, (b) Initial configuration of a grown turf with the CRW algorithm, (c) Periodic unit cell. The red segments were initially located inside the periodic cell and the blue ones are shifted into the cell.

4. Computational results and discussion

4.1 Initial turf geometry

In deciding which *statistical* parameters describe the nano-scale geometry of the turf, in a way conducive to macroscopic modeling, we are mostly guided by intuition. We begin with three parameters:

- The *tortuosity* is defined as the average curvature K (17).
- We define the *density*, ℓ , as a purely geometric parameter: the average length of CNTs per unit volume of a turf. To compute the volume, we use the average height of CNTs in a turf (cf. Figure 4).
- The *connectivity*, γ , is defined as the average number of contacts per unit length of a CNT. Total number of contacts is computed using a contact detection algorithm based on the nearest distance between the walls of neighboring tubes after relaxation. A cut-off distance of 2.54 nm is used (r_2 in Figure 3b), so that only segments within the cut-off distance were taken into account, as illustrated in Figure 5.

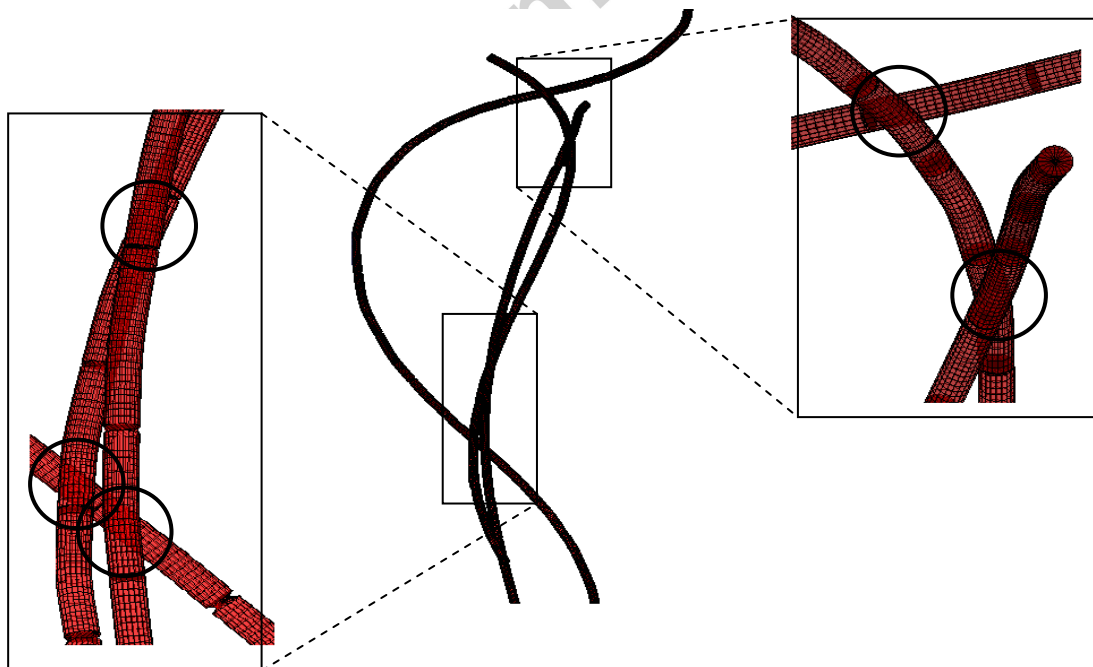


Figure 5. A typical representation of contacts between interacting CNTs, found using the contact detection algorithm, with two magnified portions (rectangular regions). The left and right boxes show details of three and two contacts, noted by black circles.

However, in generating turfs, we have only varied two *computational* parameters⁸, the seed density ρ_S and the limiting cone angle α . For this method of generating turfs, the three statistical parameters may not be independent. Nevertheless, we used all three statistical parameters, in a hope of discovering the best combination suitable for macro-scale modeling.

The dependence of statistical parameters on computational parameters is illustrated in Figure 6. It is clear that the tortuosity depends primarily on the cone angle, while line density and connectivity depend almost exclusively on the seed density. By fitting the data shown in Figure 6, and with the aid of dimensional analysis, we obtain the following empirical relations between macroscopic statistical parameters (K, ℓ, γ) and computational parameters used to generate the turf (α, ρ_S, w):

$$\begin{aligned}\frac{Kw}{\alpha} &\approx 0.23 + 0.5 \cdot 10^{-3} w^2 \rho_S, \\ \frac{\ell}{\rho_S} &\approx 0.9 + 0.14\alpha, \\ \gamma w &\approx 0.22 + 0.02 w^2 \rho_S.\end{aligned}\tag{18}$$

⁸ We did not vary the step size w , see (16) and Figure 4a.

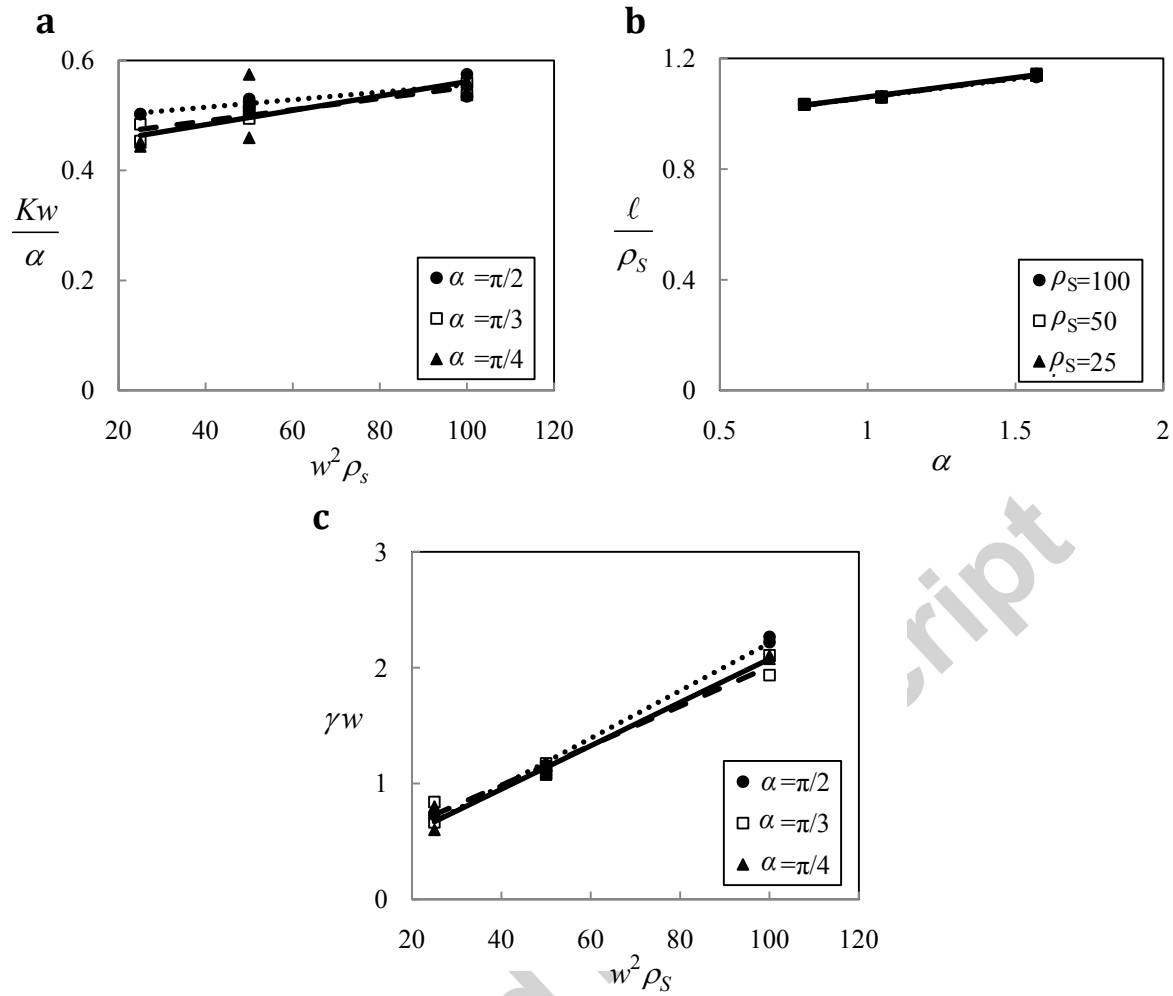


Figure 6. Relationship between statistical parameters and computational parameters used to generate the mesoscale model. (a) Tortuosity vs. seed density. (b) Density vs. cone angle. (c) Connectivity vs. seed density.

4.2 Turf deformation under uniform load

Following the relaxation, the turf is subjected to uniaxial deformation by a rigid flat punch. The nanotubes are clamped at the substrate. As soon as the initially free ends establish contact with the punch, the slip between the tubes and the punch is prevented.

The punch is moving with the constant velocity of 3 m/s, which is slow enough to ensure a macroscopically quasi-static deformation, as the energy plots in Figure 7a,c indicate. Except for the small spike following the initial contact, the kinetic energy is negligible in comparison with the strain energy. The spike is probably the result of sudden change of boundary conditions upon initial contact, resulting in unstable snapping of neighboring contacts.

The main peaks of strain energy correspond to the formation of consecutive buckled layers. Comparison with stress-strain curves, Figure 7b and d, indicates that only the formation of the first buckle is accompanied by a stress drops. The results are in qualitative agreement with experimental observations (Zbib et al., 2008; Maschmann et al., 2011). Deformed configurations of a turf at different strains are shown in Figure 8.

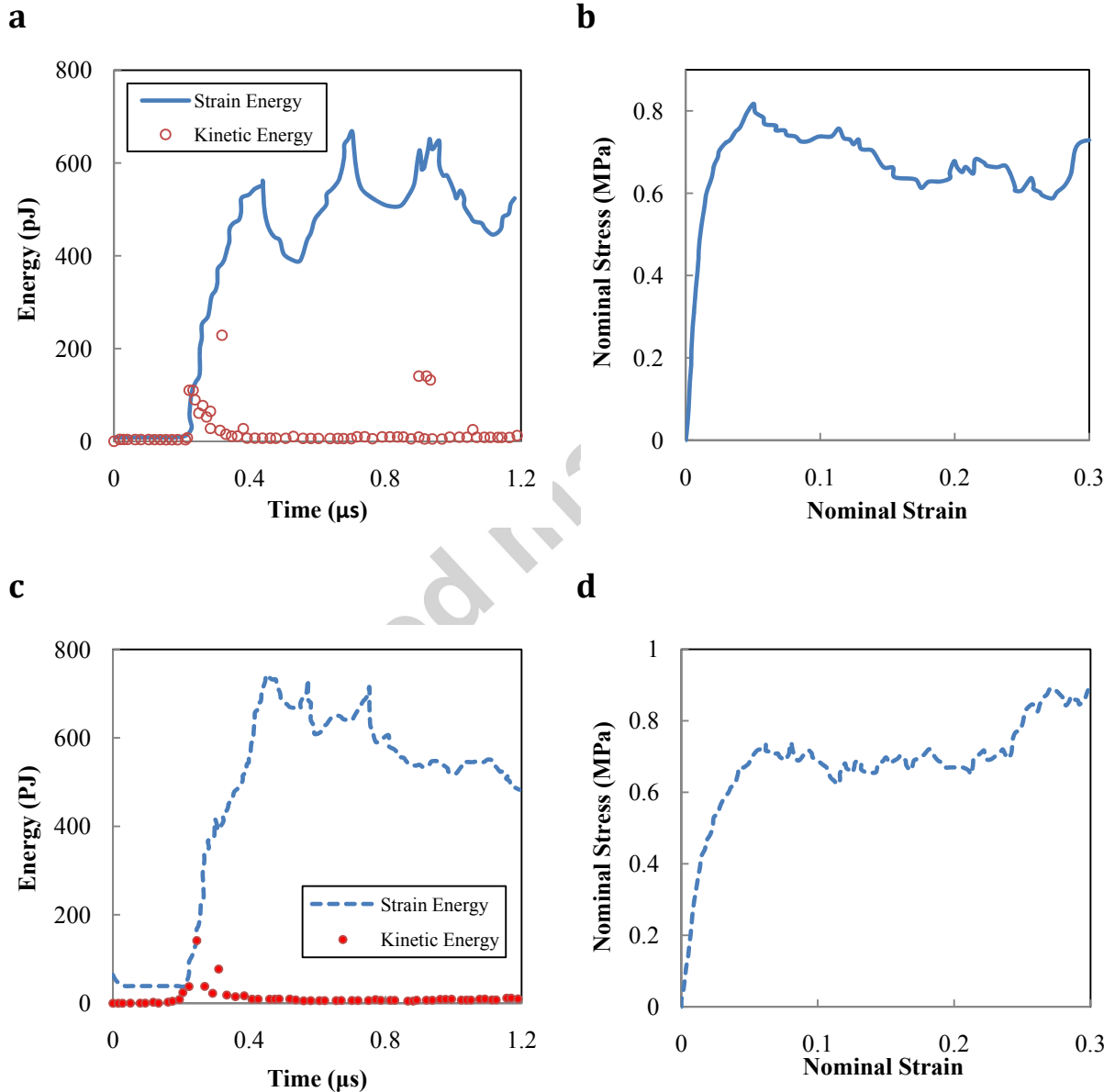


Figure 7. Turfs with 50 tubes, substrate size of $1 \times 1 \mu\text{m}^2$. **(a)** Strain energy and kinetic energy vs. time for $\alpha = \pi/8$ and **(b)** the nominal stress as a function of nominal strain. **(c)** Strain energy and kinetic energy vs. time for $\alpha = \pi/4$ and **(d)** the nominal stress as a function of nominal strain.

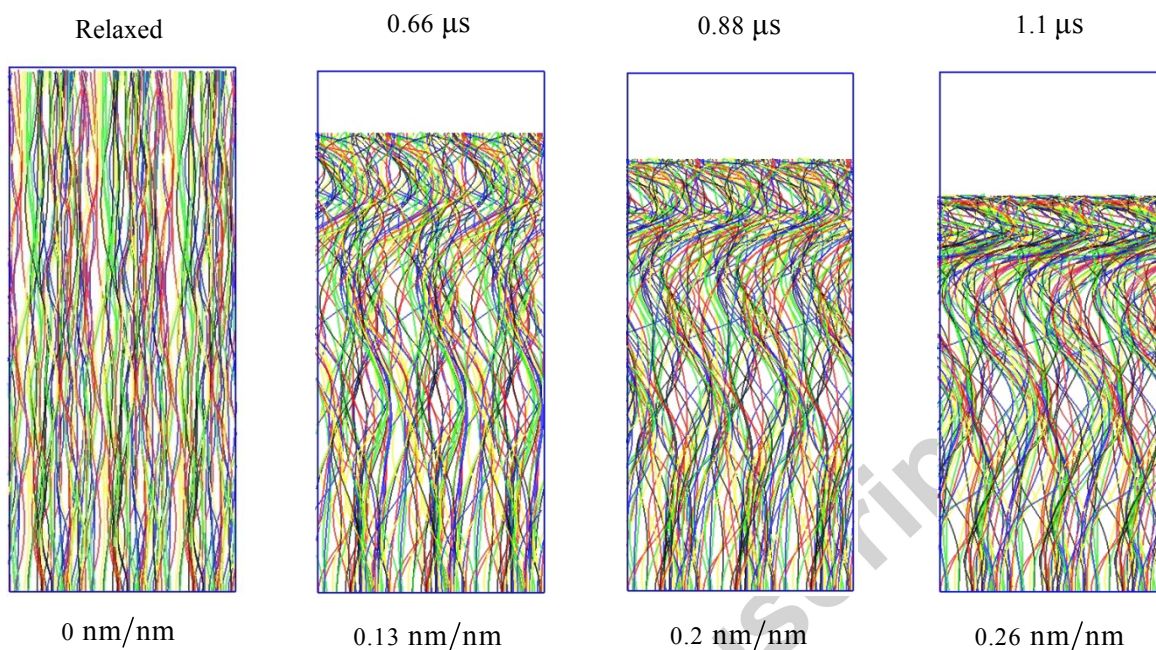


Figure 8. Deformed shape of the turf with 50 tubes, substrate size of $1 \times 1 \mu\text{m}^2$, and $\alpha = \pi/8$. Animation sequence for the case $\alpha = \pi/3$ is provided in the Supplementary material.

Experimental methods are not yet at the point where the topological measures, such as those used in Figure 6 would be available. Nevertheless, some comparison with experimental results is possible if rougher measures, such as seed or mass density of the turf are used. Broad agreement between our computational model and the experiments is illustrated in Table 2, although the computational power restricts the height of turfs in our model.

Table 2. Comparison between computational and experimental mass densities and initial elastic moduli. [1] Qiu et al., 2011a, Johnson et al., 2009, [3] Qiu and Bahr, 2013, [4] McCarter et al., 2006.

Quantity	Computational	Experimental
Seed density (tubes/ μm^2)	100	[1, 2]: 100
Mass density (g/cm^3)	0.02 ($\pm 6\%$)	[2]: 0.016-0.232; [3]: 0.13 ($\pm 20\%$)
Height of the turf (μm)	10	20-100
CNT thickness (nm)	20	10-20
Initial elastic modulus (MPa)	20-65	[1]: 50-60; [3]: 31-108; [4] 10-20

The post-buckling stress, σ_b (defined, for consistency, at the strain of 0.1), is linearly dependent on the line density, as shown in Figure 9(a). This is consistent with experimental observations by Abadi et al. (2012). In view of (18) and Figure 6b, this dependence is practically the same as dependence on seed density and is easily explained: at a given stress, the more nanotubes share the same load, the smaller the force on each tube. Beyond this dependence, we find that the randomness of the sample produces too large a scatter of results for a convincing fit⁹. This is illustrated in Figure 9b.

In Figure 10, we show the stress-strain curves for samples produced with different cone angles, where stresses are normalized by the line density. In view of the Figure 6a, the larger cone angle produces the larger curvature. Thus, from Figure 10, we conclude that higher initial tortuosity results in lower initial tangent modulus of the turf. This is not surprising, as it corresponds to the buckling behavior of a single elastica: the tangential stiffness decreases with increasing curvature.

In summary, both density and tortuosity are significant contributing factors determining the initial tangent stiffness of the turf, but the density is the primary factor dictating the post-buckling stress.

⁹ We have also attempted to fit the data to a simple model based on a buckling of a representative segment, with given curvature and prescribed length determined by the connectivity, but without success. It appears that the disorder of the structure and collective nature of the buckling process are sufficiently complex to defy a simple averaging (cf. Section 4.2.2).

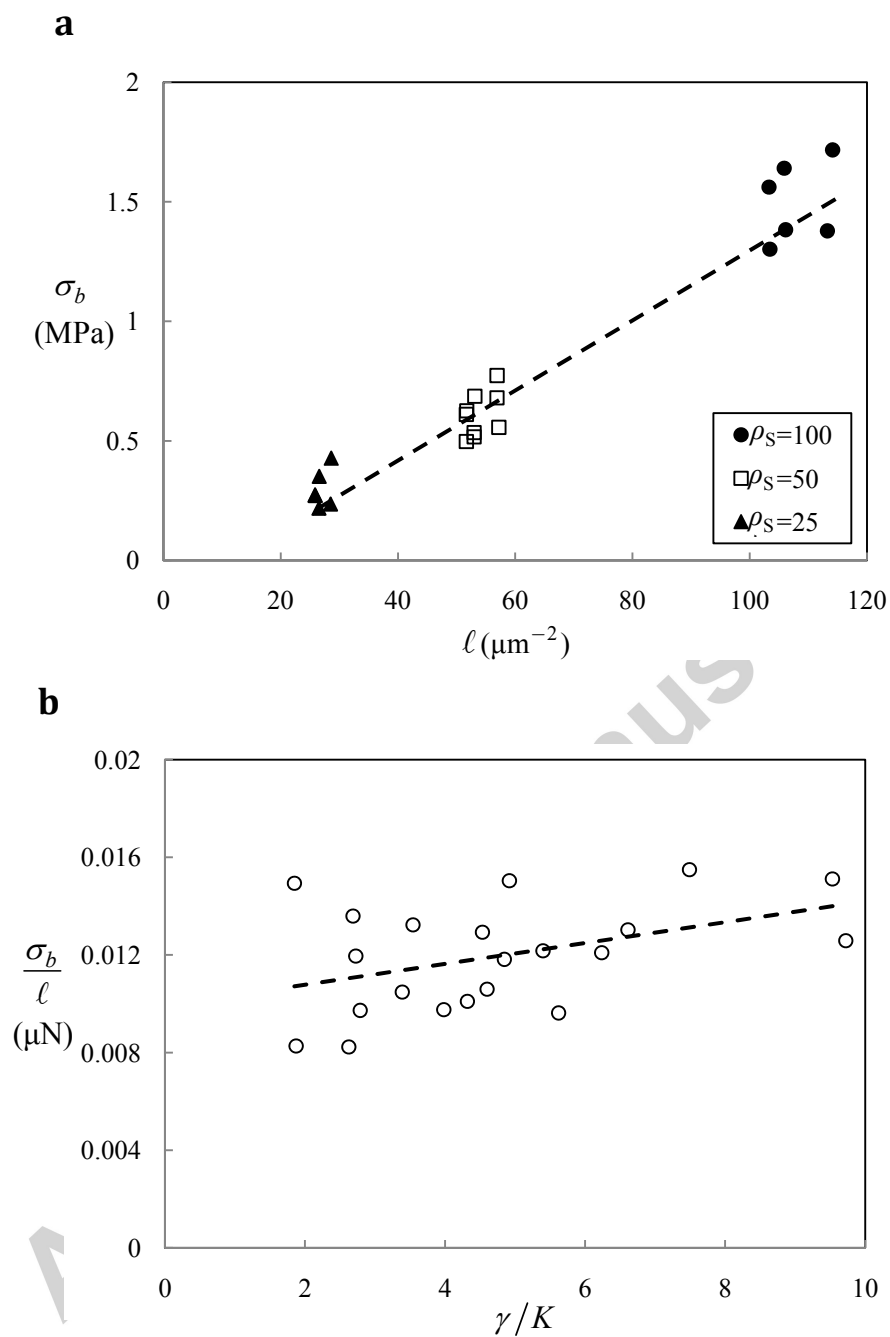


Figure 9. (a) Post-buckling stress of CNT turfs (at the strain of 0.1) as a function of line density. (b) Additional dependence of the post-buckling stress on γ/K .

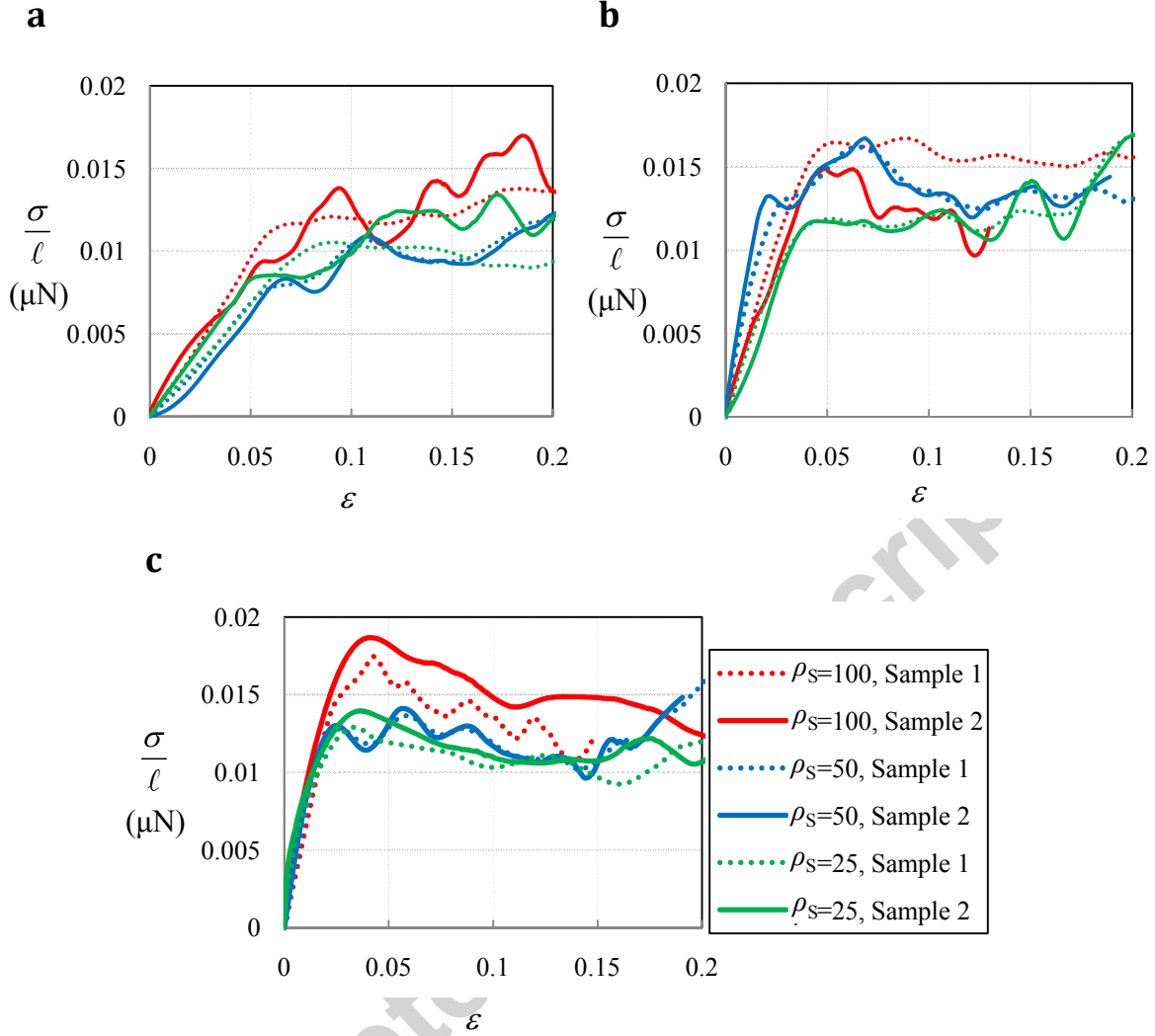


Figure 10. Stress-strain behavior of the indented turfs with various seed densities and cone angle of (a) $\pi/2$, (b) $\pi/3$, and (c) $\pi/4$. Sample 1 and sample 2 are different realizations of the random process used to generate the turf.

Experiments indicate that the buckling stress is strongly dependent on the turf height. Zbib et al (2008) conducted uniform loading experiments on CNT turfs with height 30-200 μm . Although our computations are outside that range, the simple model devised by Zbib et al (2008) fits their data well. When extrapolated to our case, and with our measured buckling wavelengths and elastic moduli, this estimate agrees with our results: $\sigma/E \approx 0.04 \div 0.07$.

4.2.2 Buckling wavelength

In order to extract the buckling wavelength from computational results, we define the half-wavelength of each tube as the distance from the indenter to the nearest point where the tangent is (nearly) vertical (Figure 11). More precisely, we find the first (from the top) minimum in the magnitude of the horizontal component of the tangent.

In Figure 12, we show a buckled turf with 9 periodic unit cells. Our results are consistent with experiments by Maschmann et al. (2011) who also observe coordinated buckling in the top portion of a turf and propagation of subsequent buckles towards the bottom substrate with increasing strain. However, in our group, we have observed the buckling initiation at the bottom (Zbib et al, 2008). While we cannot explain experimental differences, the computational results are easier to interpret. The location of the first buckle (top vs. bottom) is dictated by the weaker boundary constraint.

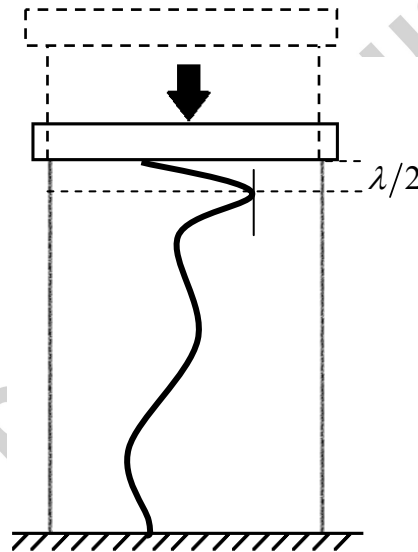


Figure 11. Schematic sketch illustrating a buckled tube under uniform compression. The buckling half-wavelength $\lambda/2$ shows the distance from the indenter surface to the first point on the elastica with nearly vertical tangent.

The influence of nano-topology on the buckling wavelength of turfs is summarized in Figure 13. We have considered all possible dependencies consistent with the dimensional analysis and the best fit is obtained as:

$$\frac{\lambda}{\sqrt{\ell}} \approx 2.22 + 1.29 \frac{\gamma}{K}; \quad \text{for: } 0.2 < \frac{\gamma}{K} < 10, \text{ and, } 25 < \ell [\mu\text{m}^{-2}] < 120. \quad (19)$$

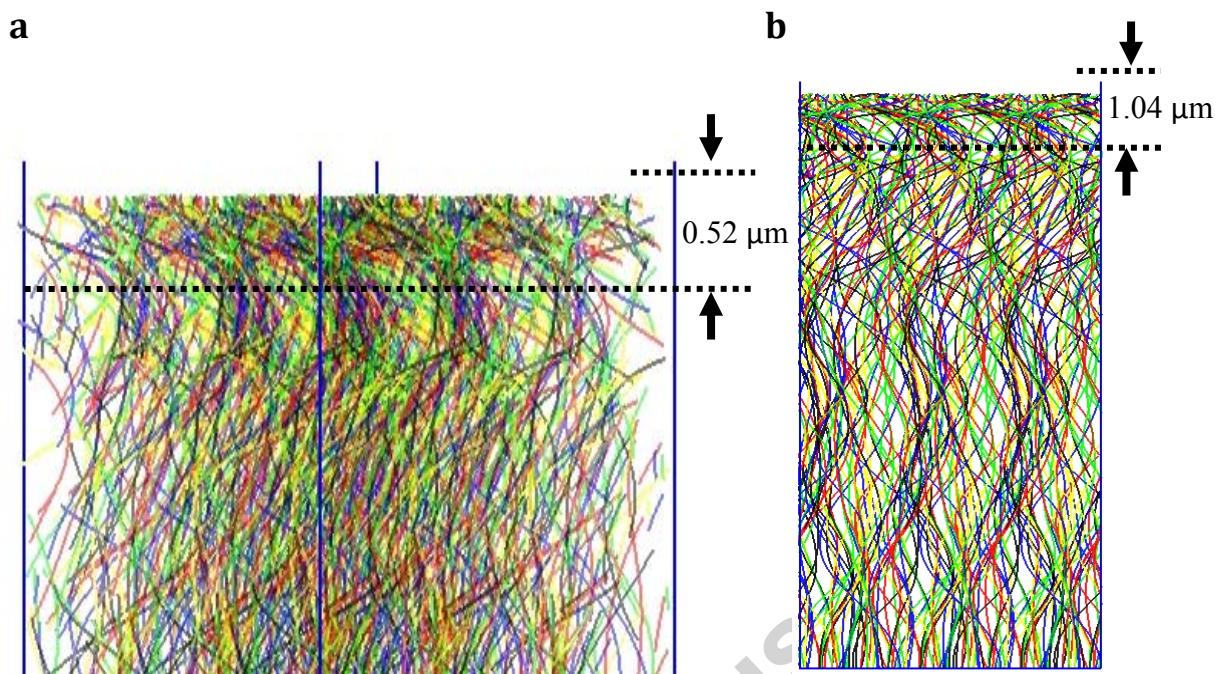


Figure 12. Buckled sample with 9 periodic unit cells (each with 50 tubes, substrate size of $1 \times 1 \mu\text{m}^2$, and $\alpha = \pi/3$) at the nominal strain equal to 0.1. **(a)** Magnified top portion of the rotated view showing the buckling half-wavelength. **(b)** Buckling wavelength from the front view.

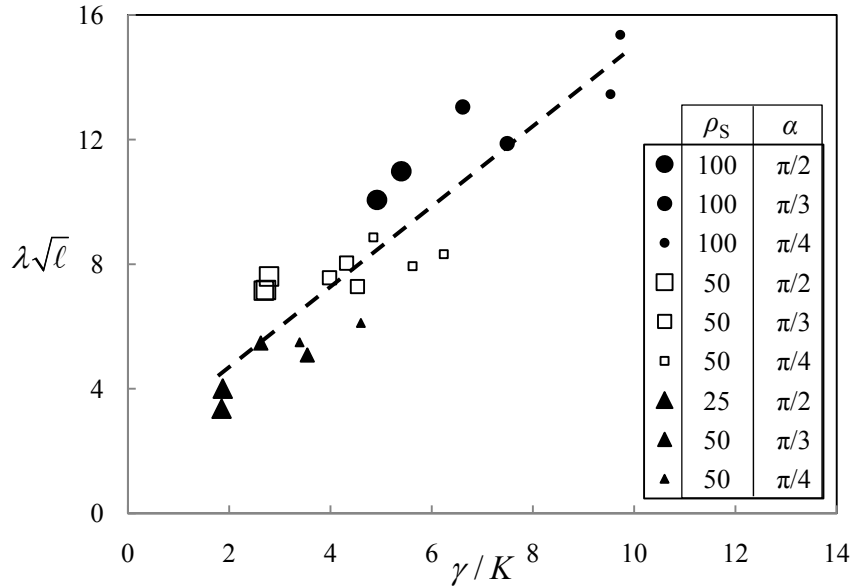


Figure 13. Buckling wavelength of CNT turfs as a function of statistical turf parameters. The buckling wavelength is determined at the nominal strain of 0.1. The statistical parameters correspond to the unloaded turf (after relaxation).

4.2.3 Reorientation of buckled segments

Experimental observations, as well as the rough model of the collective buckling (Zbib et al, 2008), indicate that, in the process of collective buckling, CNTs reorient to buckle in (approximately) the same osculatory plane.

The current computational model enables us to study this phenomenon. To that end, we consider the points corresponding to the buckling half-wavelength at the specific nominal strain (0.1). Then, we compute the bi-normals (1) at those material points for the prior times. The binormal to the curve at a point is the normal vector of the osculatory plane at that point. Ignoring the z component of the binormal, we consider the horizontal projections (onto the x - y plane), and present their orientation in the form of the rose plot (Figure 14). Before relaxation (Figure 14a), the tubes are randomly distributed in all direction. After relaxation (Figure 14b), the CNTs are oriented in a narrower range of angles, but with variation between different samples. Upon loading, the dominant directions become more pronounced (Figure 14c). Finally, after the buckling, the osculatory planes are nearly parallel, i.e., their normals span a much smaller range of orientation angles.

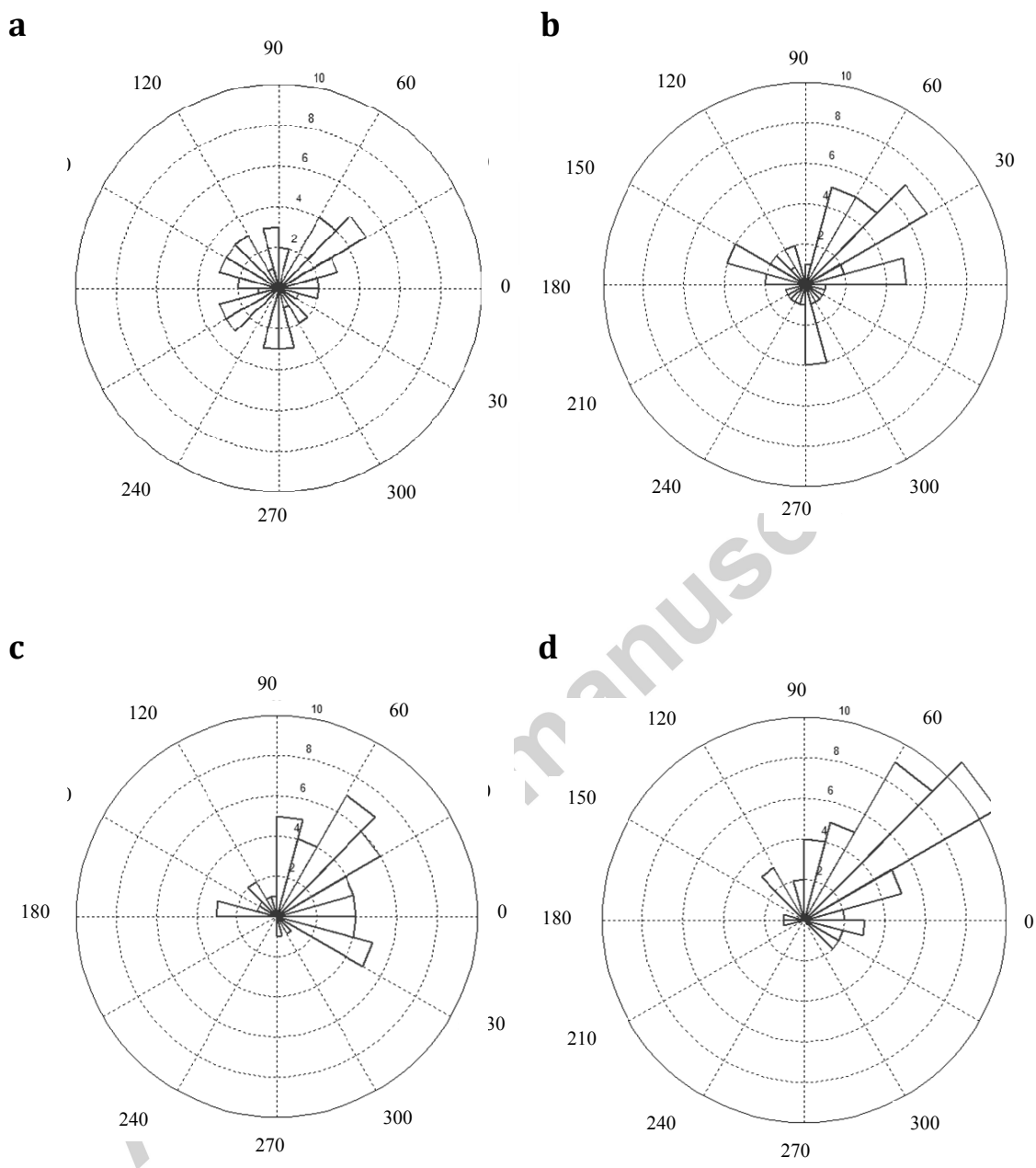


Figure 14. Rose diagram of the angle between the bi-normal projection and the x -axis for the turf with 50 tubes, substrate size of $0.707 \times 0.707 \mu\text{m}^2$, and $\alpha = \pi/4$, (a) Before relaxation, (b) After relaxation, (c) Before the occurrence of the first buckle, and (d) At the strain of 0.1.

5. Summary and conclusions

- A discrete, nano-scale model for collective behavior of CNTs in a turf is developed. The model is based on bending/buckling of inextensible elasticas, with van der Waals interactions modeled with the Lennard-Jones potential. The model is implemented into the finite element framework.
- A virtual turf, similar to experimentally observed disordered configurations, is generated using a constrained random walk algorithm starting from seed points at the substrate. The turf is then equilibrated.
- Three statistical parameters of turf geometry: tortuosity, density, and connectivity, are dependent on the numerical parameters used to generate turf. We have analyzed this dependence and established empirical relationships. The tortuosity depends primarily on the cone angle, while line density and connectivity depend primarily on the seed density.
- Periodic boundary conditions are used to simulate large turfs under uniform uniaxial deformation. The main interest in this paper is the experimentally observed collective buckling of CNTs in a turf, characterized by the peak stress, stress drop and an intrinsic material length scale manifested as the buckling wave length.
- The post buckling stress is mainly dependent on the density, but the initial elastic modulus also depends on the tortuosity.
- Dimensionally, all three statistical parameters contain length. The buckling wavelength does not depend on any single statistical parameter exclusively. By trying all the dimensionally consistent combinations, we have established a reasonable fit which describes the buckling wavelength as function of the statistical parameters.
- The reorientation of osculatory (buckling) planes, indicated by experimental observations and simple models of the collective buckling, is documented computationally.
- Future research directions include:
 - Simulations and analysis of different loading cases, to establish the parameters of the macroscopic constitutive model, and,
 - Formulation of the constitutive model with the material length scale.

Acknowledgments

The authors wish to acknowledge the financial support of the National Science Foundation under grant number CTS-0856436 and the NSF XSEDE (Extreme Science and Engineering Discovery Environment) grant number MSS120011.

Accepted manuscript

References

- Abadi, P.P.S.S., Hutchens, S.B., Greer, J.R., Cola, B.A., Graham, S., 2012. Effects of morphology on the micro-compression response of carbon nanotube forests. *Nanoscale* 4(11), 3373–80.
- Anderson, T., Akatyeva, E., Nikiforov, I., Potyondy, D., Ballarini, R., Dumitrica, T., 2010. Towards Distinct Element Method Simulations of Carbon Nanotube Systems. *ASME Journal of Nanotechnology in Engineering and Medicine* 1(4), 041009-041013.
- Antman, S.S., 1974. Kirchhoff's problem for nonlinearly elastic rods. *Quarterly of Applied Mathematics* 32(3), 221-240.
- Arias, R., 2006. Influence of roughness on the magnetostatic modes of ferromagnetic nanowires. *Physica B: Condensed Matter* 384, 25-27.
- Arroyo, M., Belytschko, T., 2003. Nonlinear mechanical response and rippling of thick multiwalled carbon nanotubes. *Physical Review Letters* 91(21), 215505.
- Arroyo, M., Belytschko, T., 2005. Continuum mechanics modeling and simulation of carbon nanotubes. *Meccanica* 40(4), 455–469.
- Bianchi, S., Comini, E., Ferroni, M., Faglia, G., Vomiero, A., Sberveglieri, G., 2006. Indium oxide quasi-monodimensional low temperature gas sensor, *Sensors and Actuators, B: Chemical* 118, 204-207.
- Bradford, P.D., Wang, X., Zhao, H., Zhu, Y.T., 2011. Tuning the compressive mechanical properties of carbon nanotube foam. *Carbon* 49(8), 2834-2841.
- Buehler, M.J., 2006. Mesoscale modeling of mechanics of carbon nanotubes: Self-assembly, self-folding and fracture. *Journal of Materials Research* 21(11), 2855-2869.
- Cao, A., Dickrell, P.L., Sawyer, W.G., Gahasemi-Nejhad, M.N., Ajayan, P.M., 2005. Super-compressible foamlike carbon nanotube films. *Science* 310(5752), 1307-1310.
- Chlebny, I., Doudin, B., Ansermet, J., 1993. Pore size distributions of nanoporous track-etched membranes. *Nanostructured Materials* 2(6), 637-642.
- Christensen, A.O., Jacob, J.P., Richards, C.D., Bahr, D.F., Richards, R.F., 2003. Fabrication and characterization of a liquid-metal micro-droplet thermal switch. In *Transducers, Solid-State Sensors, Actuators and Microsystems, 12th International Conference on* 2, 1427-1430 IEEE 69.
- Cola, B.A., Xu, J., Cheng, C., Xu, X., Fisher, T.S., 2007. Photoacoustic characterization of carbon nanotube array thermal interfaces. *Applied Physics* 101(5), 054313-054321.
- Comini, E., Faglia, G., Sberveglieri, G., Pan, Z., Wang, Z.L., 2002. Stable and highly sensitive gas sensors based on semiconducting oxide nanobelts. *Applied Physics Letters* 81, 1869-1871.
- Cook, E.H., Buehler, M.J., Spakovszky, Z.S. 2013 Mechanism of friction in rotating carbon nanotube bearings. *J. Mech. Phys Solids* 61, 652-673.
- Dresselhaus, M.S., Dresselhaus, G., Eklund, P.C., 1996. *Science of fullerenes and carbon nanotubes: their properties and applications*. Academic Press: San Diego
- Fraige, F.Y., Langston, P.A., 2004. Integration schemes and damping algorithms in distinct element models. *Advanced Powder Technology*, 15(2), 227-245.

- Fraternali, F., Blesgen, T., Amendola, A., Daraio, C., 2011. Multiscale mass-spring models of carbon nanotube foams. *Journal of the Mechanics and Physics of Solids* 59(1), 89-102.
- Hahm, J., Lieber, C.M., 2004. Direct Ultrasensitive Electrical Detection of DNA and DNA Sequence Variations Using Nanowire Nanosensors. *Nano Letters* 4(1), 51-54.
- Hutchens, S.B., Hall, L.J., Greer, J.R., 2010. In situ mechanical testing reveals periodic buckle nucleation and propagation in carbon nanotube bundles. *Advanced Functional Materials* 20(14), 2338–2346.
- Hutchens S.B., Needleman A., Greer J.R., 2011. Analysis of uniaxial compression of vertically aligned carbon nanotubes. *Journal of the Mechanics and Physics of Solids* 59(10), 2227-2237.
- Johnson, R. D., Bahr, D. F., Richards, C. D., Richards, R. F., McClain, D., Green, J., & Jiao, J. (2009). Thermocompression bonding of vertically aligned carbon nanotube turfs to metalized substrates. *Nanotechnology*, 20(6), 065703.
- Kim, S.H., Mulholland, G.W., Zachariah, M.R., 2009. Density measurement of size selected multiwalled carbon nanotubes by mobility mass characterization. *Carbon* 7(5), 1297–30.
- Kudin, K.N., Scuseria, G.E., Yakobson, B.I., 2001. C₂F, BN, and C nanoshell elasticity from ab initio computations. *Physical Review B* 64, 235406.
- Li, Z., Chen, Y., Li, X., Kamins, T.I., Nauka, K., Williams, R.S., 2004. Sequence-Specific Label-Free DNA Sensors Based on Silicon Nanowires. *Nano Letters* 4 (2), 245 -247.
- Love, A.E.H., 2013. *A treatise on the mathematical theory of elasticity*. Cambridge University Press.
- Maschmann, M.R, Zhang, Q., Du, F., Dai, L., Baur, J., 2011. Length dependent foam-like mechanical response of axially indented vertically oriented carbon nanotube arrays. *Carbon* 49(2), 386-397.
- McCarter, C.M., Richards, R.F., Mesarovic, S.Dj., Richards, C.D., Bahr, D.F., McClain, D., Jiao, J., 2006. Mechanical Compliance of Photolithographically Defined Vertically Aligned Carbon Nanotube Turf. *Journal of Materials Science* 41(23), 7872-7878.
- Mesarovic, S.Dj., McCarter, C.M., Bahr, D.F., Radhakrishnan, H., Richards, R.F., Richards, C.D., McClain, D., Jiao, J., 2007. Mechanical behavior of a carbon nanotube turf. *Scripta materialia* 56(2), 157-160.
- Nardelli, M.B., Fattebert, J.L., Orlikowski, D., Roland, C., Zhao, Q., Bernholc, J., 2000. Mechanical properties, defects and electronic behavior of carbon nanotubes. *Carbon* 38, 1703–1711.
- Nordgren, R.P., 1974. On computation of the motion of elastic rods. *Journal of Applied Mechanics* 41, 777.
- Ohgai, T., Mizumoto, M., Nomura, S., Kagawa, A., 2006. Single crystalline ferromagnetic metal nanowires electrodeposited into nanoporous polycarbonate films. *Journal of Surface Science and Nanotechnology* 4, 1-5.
- Pantano, A., Parks, M.D., Boyce, M.C., 2004. Mechanics of deformation of single- and multi-wall carbon nanotubes. *Journal of the Mechanics and Physics of Solids* 52(4), 789-821.

- Qi, H.J., Teo, K.B.K., Lau, K.K.S., Boyce, M.C., Milne, W.I., Robertson, J., Gleason, K.K., 2003. Determination of mechanical properties of carbon nanotubes and vertically aligned carbon nanotube forests using nanoindentation. *Journal of the Mechanics and Physics of Solids* 51(11-12), 2213-2237.
- Qiu, A., Bahr, D. F. 2013 The role of density in the mechanical response of CNT turfs. *Carbon*, 55, 335-342.
- Qiu, A., Bahr, D.F., Zbib, A.A., Bellou, A., Mesarovic, S.Dj., McClain, D., Hudson, W., Jiao, J., Kiener, D., Cordill, M.J., 2011a. Local and nonlocal behavior of CNT turfs and coordinated buckling of turf layers. *Carbon* 49(4), 1430-1438.
- Qiu, A., Fowler, S.P, Jiao, J., Kiener, D., Bahr, D.F., 2011b. Time-dependent contact behavior between diamond and a CNT turf. *Nanotechnology* 22(29), 295702-295709.
- Radhakrishnan, H., Mesarovic, S.D., 2009. Adhesive contact of elastic spheres revisited: numerical models and scaling. *Proceedings of the Royal Society A: Mathematical, Physical and Engineering Science* 465(2107), 2231-2249.
- Radhakrishnan, H., Mesarovic, S. D., Qiu, A., Bahr, D. F., 2013. Phenomenological constitutive model for a CNT turf. *International Journal of Solids and Structures* 50(14), 2224-2230.
- Ryckaert, J.P, Ciccotti, G., Berendsen, H.J.C., 1977. Numerical Integration of the Cartesian Equations of Motion of a System with Constraints: Molecular Dynamics of n-Alkanes. *Journal of Computational Physics* 23, 327-341.
- Volkov A. N., Simov K. R., Zhigilei L.V., 2009. Mesoscopic simulation of self-assembly of carbon nanotubes into a network of bundles. In *Proceedings of the 47th AIAA Aerospace Sciences Meeting, AIAA paper, 1544, 2009.*
- Wang, Q. H., Yan, M., Chang, R.P.H., 2001. Flat panel display prototype using gated carbon nanotube field emitters. *Applied Physics Letters* 78(9), 1294-1296.
- Waters, J.F., Riester, L., Jouzi, M., Guduru, P.R., Xu, J.M., 2004. Buckling instabilities in multiwalled carbon nanotubes under uniaxial compression. *Applied Physics Letters* 85(10), 1787-1789.
- Yakobson, B.I., Brabec, C.J., Bernholc, J., 1996. Nanomechanics of carbon tubes: Instability beyond linear response. *Physical Review Letters* 76, 2511-2514.
- Zbib, A.A., Mesarovic, S.Dj., Lilleodden, E., McClain, D., Jiao, J., Bahr, D., 2008. Coordinated buckling of carbon nanotube turfs under uniform compression. *Nanotechnology* 19(17), 1757-1763.

Appendix A. Finite element implementation

Finite element formulation of a bending/buckling elastica requires C^1 interpolation. We discretize the position vector of the central axis using cubic Hermite polynomials. With quadratic interpolation for the Lagrange multiplier λ enforcing inextensibility, the elastica element has 17 degrees of freedom: 8 at each end node and one at the central node (Figure A.1). Degrees of freedom at the end nodes include: 3 components of the position vector, 3 components of the unit tangent, the twist angle, and the Lagrange multiplier.

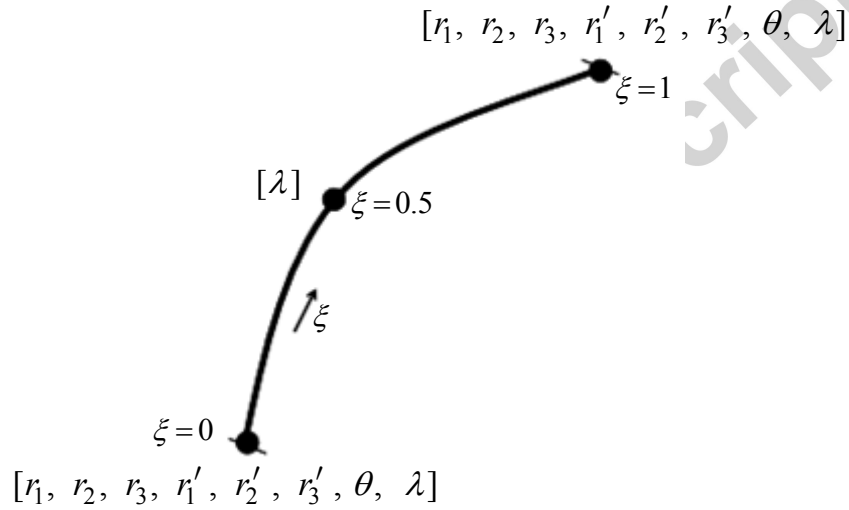


Figure A.1. Schematic of an elastica with the nodal degrees of freedom.

In the absence of distributed moments, the torsional moment must be constant in each element (4) and consequently, constant in a sequence of element that form a nanotube. Since no torsional moment is applied at the end of a tube, we can take it to be zero. In the absence of distributed loads, the weak form (3), together with suitably re-written inextensibility condition, has the form:

$$\int_0^L [B\mathbf{r}'' \cdot \delta\mathbf{r}'' + \lambda\mathbf{r}' \cdot \delta\mathbf{r}' + \rho\dot{\mathbf{r}} \cdot \delta\mathbf{r}] ds = [\mathbf{F} \cdot \delta\mathbf{r} + (\mathbf{M} \times \mathbf{r}') \cdot \delta\mathbf{r}']_0^L. \quad (\text{A.1})$$

$$\int_0^L \delta\lambda\mathbf{r}' \cdot \dot{\mathbf{r}} ds = 0. \quad (\text{A.2})$$

The FE interpolation is written as

$$r_i(s,t) = \sum_{j=1}^{12} D_i^j(s) d^j(t); \quad \lambda(s,t) = \sum_{j=1}^3 P^j(s) \lambda^j(t). \quad (\text{A.3})$$

where d^j and λ^j are the nodal degrees of freedom:

$$\begin{aligned} d^1 &= r_1(0,t); & d^2 &= r_2(0,t); & d^3 &= r_3(0,t); & d^4 &= r_1'(0,t); \\ d^5 &= r_2'(0,t); & d^6 &= r_3'(0,t); & d^7 &= r_1(L,t); & d^8 &= r_2(L,t); \\ d^9 &= r_3(L,t); & d^{10} &= r_1'(L,t); & d^{11} &= r_2'(L,t); & d^{12} &= r_3'(L,t); \\ \lambda^1 &= \lambda(0,t); & \lambda^2 &= \theta(L,t); & \lambda^3 &= \theta(L/2,t). \end{aligned} \quad (\text{A.4})$$

The lower indices which signify elements of a tensor; in subsequent equations we keep the summation convention for lower indices. The upper indices represent elements of a matrix and are summed over explicitly. The elements of the interpolation matrix $[D]$ are given in terms of Hermite cubic polynomials, while the Lagrange multiplier is represented by quadratic polynomials. Both sets of polynomials are functions of the non-dimensional arc length, $\xi = s/L$:

$$[D] = \begin{bmatrix} N^1 & 0 & 0 & N^2 L & 0 & 0 & N^3 & 0 & 0 & N^4 L & 0 & 0 \\ 0 & N^1 & 0 & 0 & N^2 L & 0 & 0 & N^3 & 0 & 0 & N^4 L & 0 \\ 0 & 0 & N^1 & 0 & 0 & N^2 L & 0 & 0 & N^3 & 0 & 0 & N^4 L \end{bmatrix}; \quad (\text{A.5})$$

$$\begin{aligned} N^1 &= 1 - 3\xi^2 + 2\xi^3; & N^2 &= \xi - 2\xi^2 + \xi^3; & N^3 &= 3\xi^2 - 2\xi^3; & N^4 &= -\xi^2 + \xi^3; \\ P^1(s) &= 1 - 3\xi + 2\xi^2; & P^2(s) &= 4\xi(1 - \xi); & P^3(s) &= \xi(2\xi - 1). \end{aligned}$$

With the variations δd^j and $\delta \lambda^j$ subject to the same interpolation, the weak form (A.1) applied on an element, is transformed into:

$$\sum_{k=1}^{12} \delta d^k \sum_{j=1}^{12} \left\{ d^j \left[B \int_0^L D_i^{k''} D_i^{j''} ds + \sum_{m=1}^3 \lambda^m \int_0^L D_i^{k'} D_i^{j'} P^m ds \right] + \ddot{d}^j \rho \int_0^L D_i^k D_i^j ds + f^k \right\} = 0 \quad (\text{A.6})$$

where f^k are suitably arranged nodal forces and moments.

For arbitrary variation δd^k , the element equations can be written as:

$$\sum_{j=1}^{12} m^{kj} \ddot{d}^j = f^k(d) + h^k(d, \lambda); \quad k = 1, \dots, 12, \quad (\text{A.7})$$

where

$$m^{kj} = \rho \int_0^L D_i^k D_i^j ds, \quad (A.8)$$

$$h^k(d, \lambda) = - \sum_{j=1}^{12} d^j \left[B \int_0^L D_i^{k''} D_i^{j''} ds + \sum_{m=1}^3 \lambda^m \int_0^L D_i^{k'} D_i^{j'} P^m ds \right].$$

The discretized form of the constraint equation (A.2) is:

$$\sum_{m=1}^3 \delta \lambda^m \sum_{k=1}^{12} \sum_{j=1}^{12} d^j \dot{d}^k \int_0^L P^m D_i^{j'} D_i^{k'} ds = 0., \quad (A.9)$$

From (A.8, A.19), the standard assembly of global matrices yields the global equations:

$$\begin{aligned} [M] \{\ddot{U}\} &= \{F(U)\} + \{H(U, \Lambda)\}, \\ [G(U, \dot{U})] &= 0, \end{aligned} \quad (A.10)$$

where $\{U\}$ is the global vector of nodal variables. These are integrated using the half-step leapfrog Verlet algorithm (Fraige and Langston, 2004), with inextensibility constraint enforced by iterative SHAKE algorithm (Ryckaert et al., 1977). Small, mass-proportional damping (damping ratio 0.05) is included for the purpose of numerical integration and to control the high frequency vibrations of the tubes. The explicit integration scheme is parallelized. The data decomposition technique is used by assigning a set of nanotubes to a particular processor during the entire simulation, so that all the processor cores are equally loaded minimizing their idle time. Communication between the cores is only necessary at the start of each time increment. The computational parameters are given in Table A.1.

Table A.1. Computational specifications of the discrete model

Degrees of freedom	Time step (sec.)	Time periods (sec.)	
		Relaxation	Indentation
45400	2×10^{-12}	2×10^{-7}	2×10^{-6}

Test case. To examine the validity of the developed FE solution, we consider the buckling of a clamped-free elastica subjected to load P (Figure A.2). The elastica is discretized using 10 elements. The comparison between the FE and the exact solutions is presented in Table A.2, where the vertical point load is normalized with respect to the

critical buckling load P_{cr} and errors are calculated for the angle (θ) between the unit tangent vector $\hat{\mathbf{t}}$ at the free end and the vertical load. It is shown that our proposed FE solution is in good agreement with the analytical solution.



Figure A.2. Schematic of a clamped-free elastica subjected to a vertical point load.

Table A.2. Comparison of numerical and exact results

P/P_{cr}	Error in θ (%)
1.02	0.085
2.54	0.083
9.11	0.065

Appendix B. Parameters

The value of elastic modulus E is based on Jacobson et al. (1996) ab initio calculations. The inner and outer radius of the tubes is estimated from Qui et al. (2011a) SEM results, and the values correspond to 5-wall nanotubes.

The bending stiffness B (2), is calculated for a cylindrical beam as

$$B = EI = E \frac{\pi}{4} \left[\left(R + \frac{h}{2} \right)^4 - \left(R - \frac{h}{2} \right)^4 \right]. \quad (\text{B. 1})$$

where R and h are the radius of the wall centerline and the thickness of the CNT wall.

The mass per unit length, ρ in (4), is determined from Kim et al. (2009) estimates of mass density (per unit volume) of multiwall CNTs, and geometric parameters. The parameters are listed in Table B.1.

The parameters of the Lennard-Jones potential (13), are based Buehler's (2006) estimate for a single wall CNT, and scaled to represent the change in contact area (outer surface) per unit length of a CNT, and multiple walls. This is a rough, order-of magnitude estimate. The reference velocity v_0 in (15) is assumed to be a fraction of the indenter speed during loading of the turf.

Table B.1. Geometric and mechanical parameters of the model.

Parameter	Value	Parameter	Value
Number of walls	5	Elastic modulus	4.0 N/nm ²
Inner diameter	16.6 nm	Bending stiffness	1.65 × 10 ⁻³ Nnm ²
Outer diameter	20.0 nm	Mass per unit length	1.86 × 10 ⁻¹ ng/m
ε/σ	4.5 nN	σ	1.163 nm
μ	1.0	v_0	1 m/s
β	0.1		

Reported experimental and computational results regarding the friction between CNTs/graphene sheets have been recently summarized by Cook et al. (2013). They vary by several orders of magnitude. Our choice is phenomenological, aimed at qualitative agreement with observations, as follows:

- (1) For the friction coefficient much smaller than 1, no collective buckling is observed in our simulations. The vibrational energy of CNTs remains high (cf. Figure 7) and numerical convergence is difficult to achieve. It is clear that the numerical system is under-constrained compared to the physical system.
- (2) Large coefficient of friction leads to fixed contacts, and removes any dissipation from the system, contrary to experimental observations (Qiu et al, 2011b).
- (3) For the friction coefficient of the order 1, the behavior corresponds to the experimental observations. Moreover, it is relatively insensitive to the changes by factor 2, as illustrated in Figure B.1.

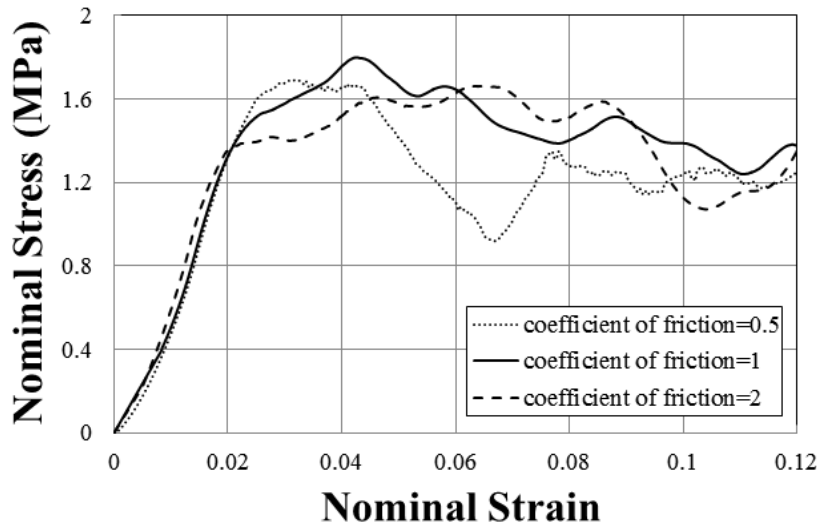


Figure B.1. Effects of moderate changes in the coefficient of friction on stress-strain behavior.

- Nano-scale model: collective behavior of CNTs in a turf. Van der Waals interactions.
- Virtual turfs with 3 statistical parameters: tortuosity, density, connectivity.
- Collective buckling of a layer under uniform load: The buckling stress.
- The buckling wavelength is an intrinsic material length scale.
- The buckling mechanism: reorientation of osculatory (buckling) planes.

Accepted manuscript